Temperature-driven band inversion in $Pb_{0.77}Sn_{0.23}Se$: Optical and Hall effect studies

Naween Anand, Sanal Buvaev, A. F. Hebard, and D. B. Tanner
Department of Physics, University of Florida, Gainesville, Florida 32611-8440, USA

Zhiguo Chen and Zhiqiang Li
NHMFL Florida State University, Tallahassee, Florida 32310-3706, USA

Kamal Choudhary and S. B. Sinnott
Department of Materials Science and Engineering, University of Florida, Gainesville, Florida 32611-8440, USA

Genda Gu
Condensed Matter Physics and Materials Science Department, Brookhaven National Laboratory, Upton, New York 11973-5000, USA

C. Martin
Department of Physics, Ramapo College, Mahwah, New Jersey 07430, USA
(Received 18 July 2014; revised manuscript received 17 November 2014; published 23 December 2014)

Optical and Hall effect measurements have been performed on single crystals of $Pb_{0.77}Sn_{0.23}Se$, a IV-VI mixed chalcogenide. The temperature-dependent (10–300 K) reflectance was measured over 40–7000 cm^{-1} (5–870 meV) with an extension to 15 500 cm^{-1} (1.92 eV) at room temperature. The reflectance was fitted to the Drude-Lorentz model using a single Drude component and several Lorentz oscillators. The optical properties at the measured temperatures were estimated via Kramers-Kronig analysis as well as by a Drude-Lorentz fit. The carriers were p type with the carrier density determined by Hall measurements. A signature of valence intraband transition is found in the low-energy optical spectra. It is found that the valence-conduction band transition energy as well as the free-carrier effective mass reach minimum values at 100 K, suggesting temperature-driven band inversion in the material. Density functional theory calculations for the electronic band structure are also presented.

DOI: 10.1103/PhysRevB.90.235143 PACS number(s): 78.20.−e, 78.40.Fy

I. INTRODUCTION

Class IV-VI narrow-gap compound semiconductors have been of great interest for many decades not only for their scientific interest but also for their use in novel technological instrumentation such as infrared optoelectronics and thermoelectric devices [1,2]. Crystallizing in the rocksalt structure, materials such as PbTe, PbSe, SnTe, and their mixed alloys have been found to have high dielectric constants and quite unusual infrared and electronic properties [3]. PbSe and SnSe, the two parent compounds of the $Pb_{1-x}Sn_xSe$ alloy system, have what is commonly known as band inversion [4]. For $x = 0$, i.e., PbSe has L_6^- symmetry for the conduction band while the valence band symmetry is denoted by L_6^+, a topologically trivial phase. As one increases x in the alloy system, $Pb_{1-x}Sn_xSe$, the band gap initially reduces and then closes at $x = 0.38$, with a linear dispersion around the Fermi level. Subsequent increases in x, to $0.38 \leqslant x \leqslant 0.43$, lead to the gap reopening at the L point; now the valence band symmetry gets inverted to L_6^-, whereas the symmetry of the conduction band changes to L_6^+, a topologically nontrivial phase.

Recent theoretical and experimental interest in these alloys has occurred because they have been suggested to represent a new, nontrivial topological phase called a topological crystalline insulator (TCI) [5,6]. As in most topological insulators, observations are complicated because the crystals are usually found to be either p doped or n doped due to nonstoichiometry so that surface-state features get overshadowed by an overwhelming bulk-carrier contribution. This is the case in the data reported here. Nevertheless, the temperature dependence of the free-carrier effective mass and of the valence-to-conduction band absorption edge could be a suitable point of inquiry to explore band inversion and the temperature-driven phase transition in such materials. In fact, a pressure-induced topological phase transition has been recently observed and studied in this material [7]. So, apart from determining the optical and transport properties, this study also attempts to investigate such a possibility in a $Pb_{0.77}Sn_{0.23}Se$ single crystal.

Optical reflectance and transmittance measurements over a wide frequency range have been performed along with band-structure calculations for PbS, PbSe, and PbTe many years in the past [8–10]. These studies find that the materials are small band gap semiconductors doped either n or p type due to crystal defects. Structural studies of PbSe have reported the rocksalt crystal structure at ambient temperature and pressure with a lattice parameter of $a = 6.13$ Å and a direct minimum energy band gap of around 0.28 eV at the L point in the Brillouin zone [3,11,12]. In contrast, SnSe has been stabilized as an orthorhombic crystal with layered symmetry and an indirect minimum energy band gap of 0.9 eV [3,13]. On the basis of x-ray diffraction studies of annealed powders, it has been established [14,15] that the mixed alloy $Pb_{1-x}Sn_xSe$ stabilizes in the rocksalt structure for $0 \leqslant x \leqslant 0.43$ and that the minimum band gap remains at the L point. Infrared absorption measurements [16] find that the gap is a complex function of temperature and stoichiometric ratio x. An ARPES study [17] of $Pb_{0.77}Sn_{0.23}Se$ finds that the band

 ©2014 American Physical Society

gap is temperature dependent, with a minimum around 100 K. The bulk band gap reopens at the L point with an inverted symmetry of the valence band (L_6^-) and the conduction band (L_6^+) as the temperature is further increased [17,18].

II. EXPERIMENTAL PROCEDURES

Compositional and structural defects play a significant role in determination of chemical and electronic properties of lead chalcogenides. Local compositional disorder significantly affects the band gap formation for the alloy compositions. In addition, short-range disorder breaks the degeneracy near the band edge [19] because PbSe and SnSe represent two different crystal structures. Therefore, controlled crystal growth is an essential requirement.

Single crystals of nominal composition $Pb_{0.77}Sn_{0.23}Se$ were grown by a modified floating-zone method. High-purity (99.9999%) elements of Pb, Sn, and Se were loaded into a quartz ampoule and sealed under vacuum. The materials in the double-sealed quartz tube first were melted at 1000 °C in a box furnace and fully rocked to achieve homogeneous mixture. Then, the premelt ingot rod (12 mm in diameter and 20 cm in length) located in a quartz tube was mounted in a floating-zone furnace. In the floating-zone furnace, the ingot was first premelted at a velocity of 200 mm/hr and then grown at 1.0 mm/hr in a 1 bar Ar atmosphere. The crystals had the rocksalt structure with lattice parameter $a = 6.098$ Å. Lead chalcogenide crystals are opaque and have a metallic luster. They are brittle and easily cleave along the (100) plane. Chemical binding in these systems has both ionic and covalent components. A single crystal of size $4 \times 4 \times 2$ mm^3 with smooth (100) crystal plane as the exposed surface was selected for optical measurements.

Temperature-dependent (10–300 K) reflectance measurements were conducted using a Bruker 113v Fourier-transform interferometer. A helium-cooled silicon bolometer detector was used in the 40–650 cm^{-1} spectral range and a DTGS detector was used from 600–7000 cm^{-1}. Room temperature measurement up to 15 500 cm^{-1} used a Zeiss microscope photometer. Because the rocksalt structure of the material implies isotropic optical properties, all optical measurements were performed using nonpolarized light at near-normal incidence on the (100) crystal plane. To achieve higher accuracy during reflectance measurements, a small evaporation device incorporated in the metal shroud of the cryostat was used to coat the crystal surface with gold, minimizing changes of experimental conditions during sample and reference single-beam spectral measurements. The gold coating was easy to remove since the material is easily cleaved along the (100) plane.

Optical measurements were followed by Hall-effect measurements, using a physical properties measurement system (PPMS) from Quantum Design which allows transport measurement over 10–300 K. Magnetic fields up to 7 T were applied perpendicular to the (100) plane and ramped in the upward and downward directions while the Hall voltage was measured transverse to current and field. The Hall-effect measurements gave the sign (p type) and value for the carrier density n at 10 K and at room temperature. Errors in the carrier density estimate originate from the nonuniform thickness of the sample, nonrectangular cross section, and contact size. The errors are of course the same at each temperature. These errors do affect the discussion in a later section, where we compare Hall measurements and the infrared plasma frequency $\omega_p = \sqrt{4\pi n e^2/m_h^*}$, where e is the electronic charge and m^* is the effective mass of the holes. Our goal in this comparison is to obtain an estimate of the effective mass. In our analysis, the carrier concentration n has been linearly extrapolated over these intermediate temperatures. The volume expansion of the crystal with temperature is also included in this calculation, although it is not very significant. Because of the similarity in the crystal structure and lattice parameter, the linear thermal expansion coefficient for this material is taken to be the same as PbSe [20].

III. EXPERIMENTAL RESULTS

A. Hall effect studies

Previous Hall studies [21,22] on PbSe and SnSe reported p-type carriers in these materials. A slight increase in p-type carrier density at room temperature compared with 70 K was observed in SnSe [23]. The origin of the p-type extrinsic carrier in the crystal is due primarily to the presence of ionized lattice defects associated with deviations from nominal stoichiometry, possibly due to excess of selenium or vacancies occupied by acceptor impurities [24–26]. Our Hall measurements show p-type carriers with a concentration of $n = 6 \times 10^{19}$ cm^{-3} at room temperature. This value increases to $n = 9 \times 10^{19}$ cm^{-3} at 10 K. The relatively high value for n suggests that our sample is a degenerate semiconductor, in which the chemical potential is pushed down into the valence band due to the finite carrier density n; the location of the chemical potential (Fermi energy) is determined by the valence-band density of states.

B. Reflectance spectra

The temperature dependence of the reflectance of $Pb_{0.77}Sn_{0.23}Se$ between 40 and 7000 cm^{-1} (5 meV to 870 meV) is shown in Fig. 1. In the far-infrared range, a high reflectance is observed, decreasing somewhat as temperature increases. The effect of an optically active transverse phonon may be inferred around 40–200 cm^{-1}. This feature weakens as temperature increases [27]. The reflectance is affected by a rather wide valence intraband transition, which is centered near 660 cm^{-1} and which shifts to lower frequency with increasing temperature; this feature is evident at low temperatures and causes a modest rise in the reflectance level near the central frequency [28]. There is a plasma minimum around 930 cm^{-1} at 10 K; this feature shifts to around 885 cm^{-1} as temperature increases to 300 K and becomes slightly less deep. As we shall see, it is in good agreement with the zero crossing of the Kramers-Kronig derived real part of the dielectric function ε_1.

In the midinfrared, we observe interband transitions from the occupied states in the valence band to the conduction band. These transitions become weaker, leading to decreased reflectance, as the temperature is increased. As this is a p-type system, the chemical potential lies in the valence band; therefore, the experimentally observed minimum absorption edge in the midinfrared range is an overestimate of the direct

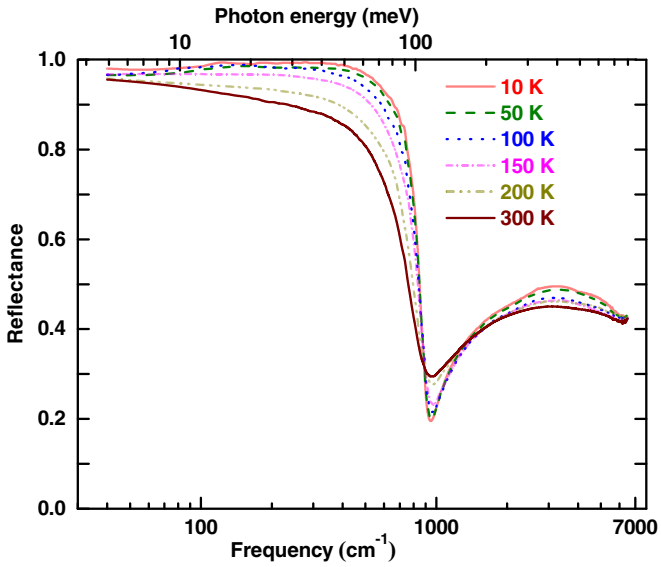

FIG. 1. (Color online) Temperature-dependent reflectance spectra of a $Pb_{0.77}Sn_{0.23}Se$ single crystal.

band gap at the L point of the Brillouin zone, which would be observed only in an intrinsic $Pb_{0.77}Sn_{0.23}Se$ crystal.

The top panel of Fig. 2 shows the 300 K reflectance up to 1.92 eV. There is a strong high-energy interband transition at 10 600 cm^{-1} (1.3 eV).

IV. ANALYSIS

A. Kramers-Kronig analysis and optical conductivity

We used the Kramers-Kronig relations to estimate the phase shift on reflection from the bulk reflectance $R(\omega)$. After this, we can calculate the real and imaginary parts of the dielectric function [29]. Before calculating the Kramers-Kronig integral, the low-frequency reflectance data were extrapolated to zero using the reflectance-fit parameters. (The fit is discussed later in this section.) Reflectance data above the highest measured frequency were extrapolated between 80 000 and 2×10^8 cm^{-1} with the help of x-ray-optics scattering functions; from the scattering function for every atomic constituent in the chemical formula and the volume/molecule (or the density) one may calculate the optical properties in the x-ray region [30,31]. A power law of $1/\omega$ was used to bridge the gap between the experimental data and the x-ray extrapolation. Finally, an ω^{-4} power law was used above 2×10^8 cm^{-1}.

The optical properties were derived from the measured reflectance and the Kramers-Kronig-derived phase shift on reflection. The lower panel of Fig. 2 shows the Kramers-Kronig-derived optical conductivity at 300 K. The narrow Drude contribution and the contributions to the conductivity from interband transitions around 3500, 5100, and 10 600 cm^{-1} are consistent with the reflectance.

The temperature dependence of the Kramers-Kronig-derived real part of the optical conductivity, $\sigma_1(\omega)$, over 50–7000 cm^{-1} is shown in Fig. 3. The far-infrared range shows the Drude contribution to $\sigma_1(\omega)$. Between 10–100 K, the Drude relaxation rate $1/\tau$ is below the measured frequency range, explaining the nonconstant area under the displayed

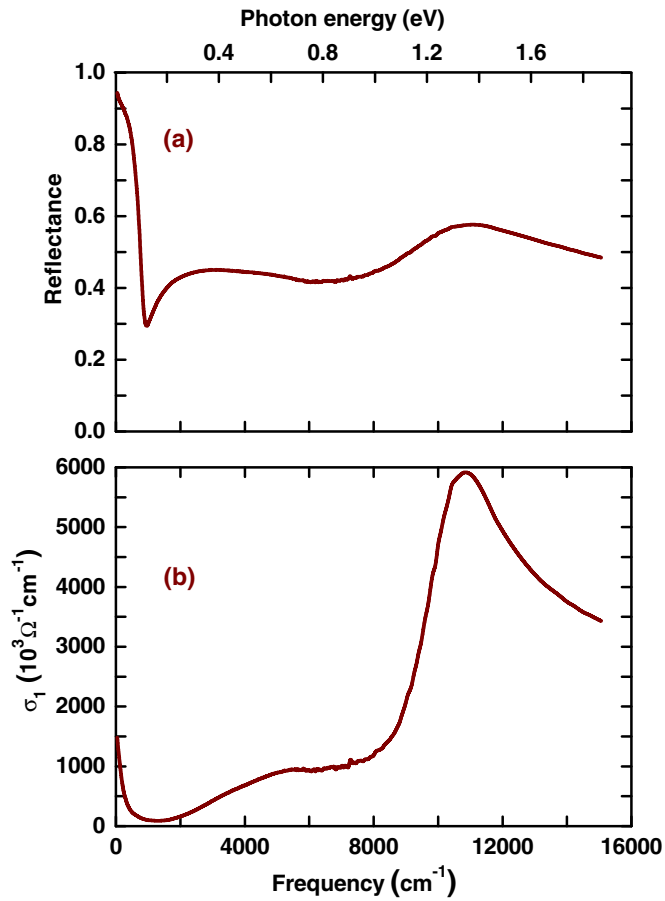

FIG. 2. (Color online) (a) Reflectance spectrum from 40 to 15 500 cm^{-1} (5 meV to 1.92 eV) at 300 K. (b) Kramers-Kronig calculated optical conductivity from 40 to 15 500 cm^{-1} (5 meV to 1.92 eV) at 300 K.

conductivity spectrum as temperature changes. The relaxation rate increases as temperature is increased until, by 200 K, most of the Drude spectral weight is seen in the figure.

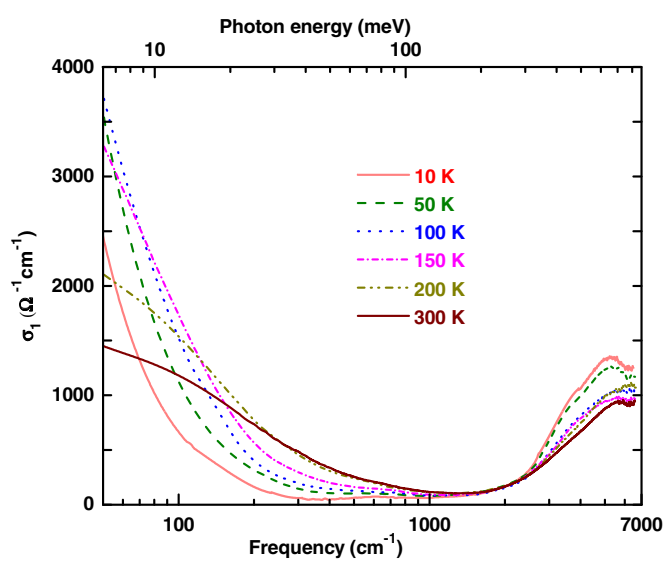

FIG. 3. (Color online) Temperature-dependent optical conductivity of $Pb_{0.77}Sn_{0.23}Se$ single crystal obtained by Kramers-Kronig analysis.

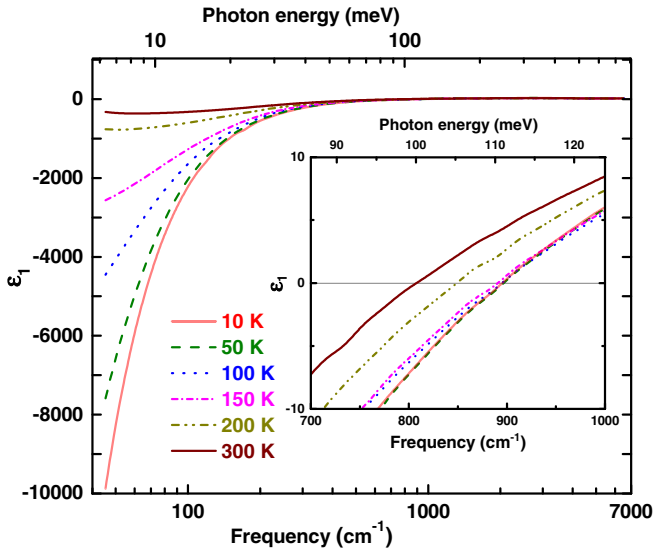

FIG. 4. (Color online) Temperature dependence of the real part of the dielectric function of $Pb_{0.77}Sn_{0.23}Se$. The inset shows the zero crossing of $\varepsilon_1(\omega)$, illustrating the temperature dependence of the screened plasma frequency.

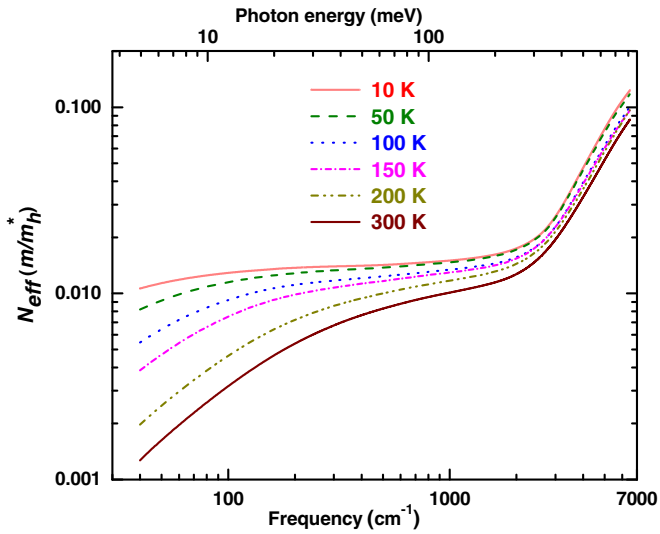

FIG. 5. (Color online) Temperature-dependent integrated spectral weight of $Pb_{0.77}Sn_{0.23}Se$.

The Drude conductivity partially overlaps with a small and dispersive contribution from the valence intraband transition at 650 cm^{-1}. This feature can be seen in the spectra at 10–100 K but becomes masked by the Drude spectrum as temperature increases. The valence intraband transition is an excitation from an occupied state below the Fermi level to an empty state (in another valence subband) above the Fermi level. It would only be observed if the Fermi level were to lie somewhere within the valence band.

In the midinfrared range, the optical conductivity decreases as temperature is increased. At most temperatures, two overlapping conductivity peaks may be discerned around 3500 and 5100 cm^{-1}; these features, arising from interband transition, are also consistent with the reflectance. The onset of the interband transitions is estimated by extrapolating linearly the conductivity to $\sigma_1(\omega) = 0$. This intercept is about 2300 cm^{-1} at 10 K, then decreases to around 2200 cm^{-1} at 100 K, and then increases back to 2300 cm^{-1} at 300 K. The temperature dependence of all parameters is discussed later.

B. The real part of the dielectric function

The Kramers-Kronig result also allows us to estimate the real part of dielectric function ε_1 shown in Fig. 4. At low frequencies, ε_1 is negative, a defining property of a metal. The temperature dependence of the free-carrier scattering rate is very evident in this dielectric function plot. For temperatures above 150 K, ε_1 becomes almost flat at low frequencies, implying that the scattering rate is on the order of a few hundred cm^{-1}. In contrast, at low temperatures $\varepsilon_1 \sim 1/\omega^2$, sharply decreasing, indicating a very small scattering rate, one below the minimum measured frequency.

The inset graph shows the zero crossing of ε_1 (representing the screened plasma frequency) for different temperatures. At 10 K the screened plasma frequency is around 900 cm^{-1}; this value is maintained to about 150 K, after which it decreases to around 815 cm^{-1} by 300 K. This Kramers-Kronig-derived screened plasma frequency is in good agreement with the reflectance plasma minimum.

C. Sum rule analysis and $N_{\text{eff}}\frac{m}{m_h^*}$

Once we have the real part of the conductivity, we can calculate the partial sum using

$$N_{\text{eff}}\frac{m}{m_h^*} = \frac{2mV_c}{\pi e^2}\int_0^{\omega}\sigma_1(\omega')d\omega' \tag{1}$$

to obtain $N_{\text{eff}}(\omega)$, the effective number of carriers participating in optical transitions up to frequency ω. The quantities in this equation are m_h^*, the hole effective mass, m, the free-electron mass, e, the electronic charge, and V_c, the volume taken up by one "molecule" of $Pb_{0.77}Sn_{0.23}Se$. Figure 5 shows the temperature-dependent partial sum rule results. The free-carrier contribution saturates around 0.015 at 10 K, decreasing to 0.011 at 300 K. These data suggest that either the carrier density is decreasing or the effective mass is increasing as temperature increases. The Hall results tell us that it is the former. We use the Hall carrier density to estimate the free-carrier effective mass and its temperature dependence. The results are shown in Fig. 6. A uniform error has been added to the data points based on the uncertainty in N_{eff} and the optical conductivity-dependent partial sum rule derived from Kramers-Kronig relations.

The effective mass changes only slightly over the range of measurements; there is a weak minimum at 100 K where $m_h = 0.335m_e$ and then a rise to $m_h = 0.350m_e$ at 300 K. The average effective mass is $\langle m_h\rangle_T = 0.341m_e$. Mass anisotropy is quite common in lead salts [32]. It is strong in PbTe, moderate in PbSe, and absent or negligible in PbS. The ratio of the longitudinal component $m_\parallel$ along the Γ-L direction and the transverse component $m_\perp$ in the plane perpendicular to Γ-L is reported to be around 1.8 in PbSe [32]. This anisotropy is expected to decrease in the heavily doped case.

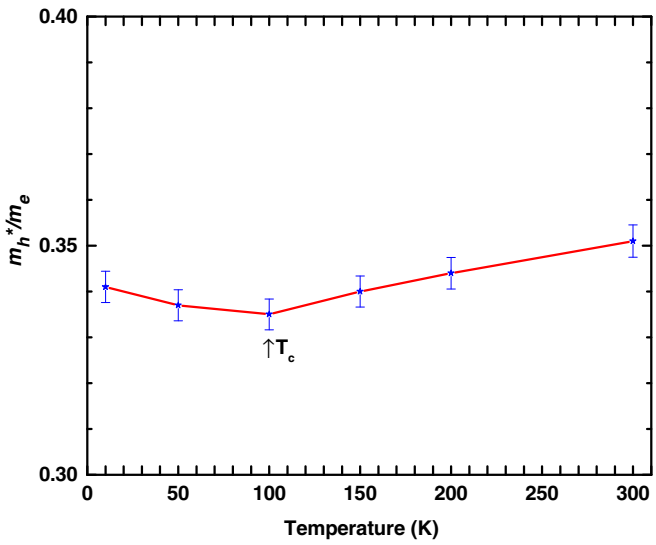

FIG. 6. (Color online) Temperature-dependent hole effective mass of $Pb_{0.77}Sn_{0.23}Se$.

In our heavily doped $Pb_{0.77}Sn_{0.23}Se$ crystal, the mass anisotropy is ignored and the above calculation assumes an isotropic effective mass. We note that on account of the doping, the Fermi level is far from the putative Dirac point and, moreover, the optical conductivity spectrum (from which this effective mass is derived) is an angular average over the Fermi surface and an energy average over a scale set by the relaxation rate, $\hbar/\tau$.

D. Energy-loss function

Finally, the temperature dependence of the longitudinal response of this material, namely the loss function $-\Im(\varepsilon^{-1})$, is plotted against frequency in Fig. 7. The free-carrier peak in the loss function is a good estimate of the screened Drude plasma

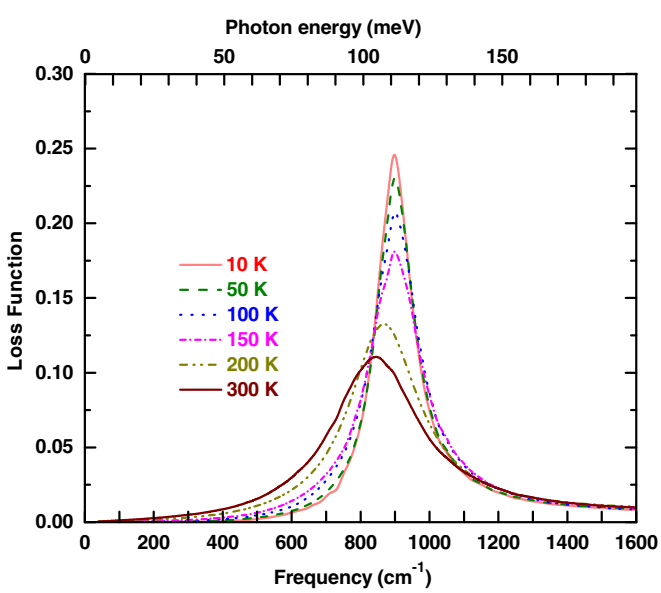

FIG. 7. (Color online) Temperature-dependent energy loss function of $Pb_{0.77}Sn_{0.23}Se$.

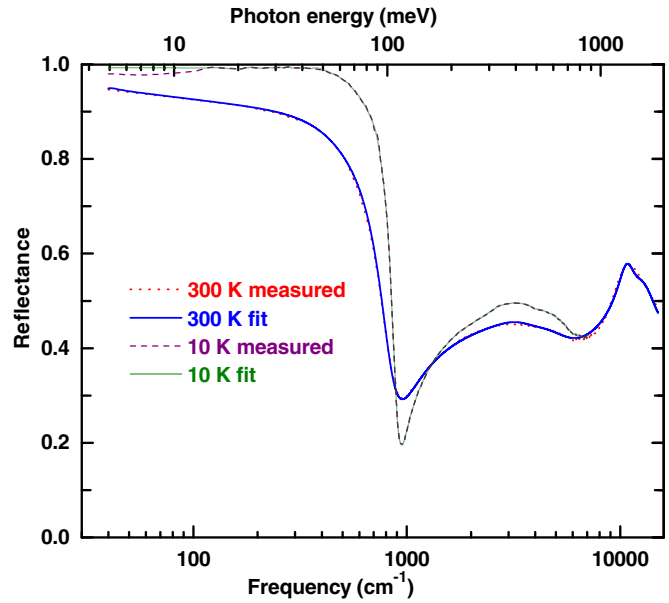

FIG. 8. (Color online) Drude-Lorentz fit to the reflectance of $Pb_{0.77}Sn_{0.23}Se$ at 300 K and 10 K.

frequency and agrees with the zero crossing of ε_1 in Fig. 4 as well as the value calculated by fitting with the Drude-Lorentz model, discussed in the next section.

E. Drude-Lorentz model fits

The Drude-Lorentz model is commonly used as a phenomenological model to fit the optical properties of both small-band-gap semiconductors such as InN and large-gap semiconductors such as GaN [33,34]. We have used this model to fit our reflectance data. The Drude component characterizes the free carriers and their dynamics at zero frequency whereas the Lorentz contributions are used both for the optically active phonon in the far-infrared region and for the valence intraband and interband transitions in the mid- and near infrared. The dielectric function is

$$\varepsilon(\omega) = \varepsilon_\infty - \frac{\omega_p^2}{\omega^2 + i\omega/\tau} + \sum_{j=1}^{6} \frac{\omega_{pj}^2}{\omega_j^2 - \omega^2 - i\omega\gamma_j}, \qquad (2)$$

where the first term represents the core electron contribution (transitions above the measured range), the second term is the free-carrier contribution, characterized by the Drude plasma frequency ω_p and the free-carrier relaxation time τ, and the third term is a sum of six Lorentzian oscillators representing phonons, valence intraband, and interband electronic contributions. The Lorentzian parameters are the jth oscillator plasma frequency ω_{pj}, its central frequency ω_j, and its linewidth γ_j. This dielectric function model is used in a least-squares fit to the reflectance.

Figure 8 compares the calculated and measured reflectance at 10 K and 300 K; the 300 K fit is shown up to 15 500 cm^{-1} whereas the 10 K data are fitted to 7000 cm^{-1}. Similar quality fits were obtained at all other temperatures.

The comparison between the Kramers-Kronig-derived and the Drude-Lorentz-model conductivity spectra at 10 K and 300 K is shown in Fig. 9. The parameters are the ones used

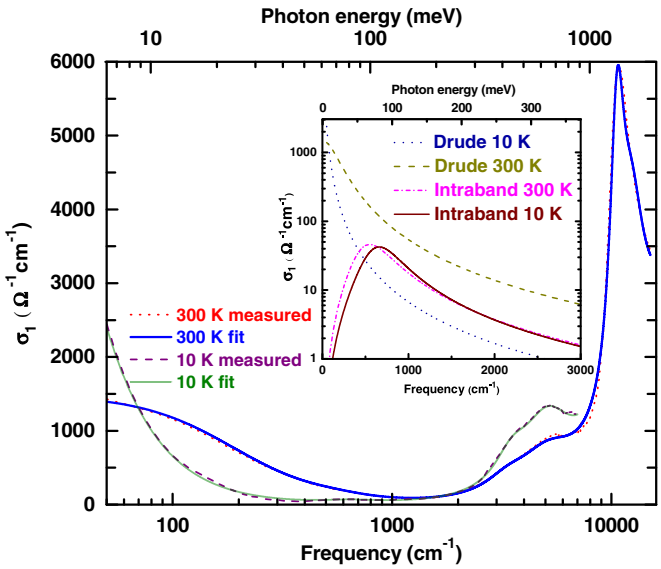

FIG. 9. (Color online) A comparison of the Kramers-Kronig-derived optical conductivity and the conductivity calculated from the Drude-Lorentz fit to the reflectance of $Pb_{0.77}Sn_{0.23}Se$. Results are shown for 10 and 300 K. The inset shows the Drude and the valence intraband contributions at the two temperatures.

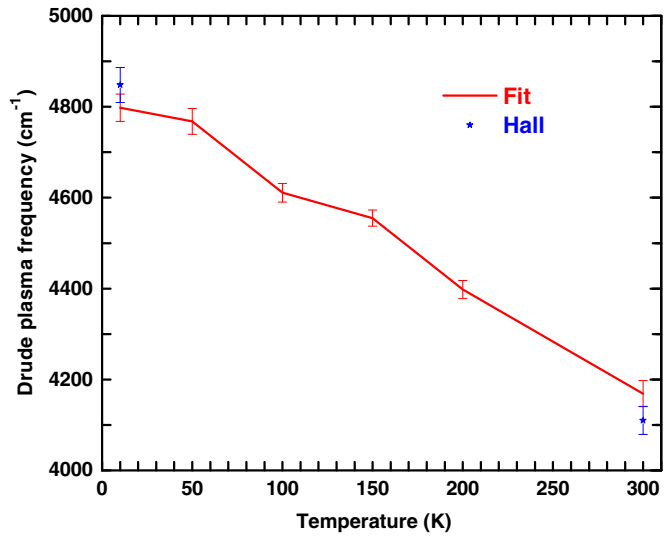

FIG. 10. (Color online) Comparison between the Drude-Lorentz model fitted and Hall-derived Drude plasma frequency (10 K to 300 K).

to fit the reflectance. That the agreement is good gives us confidence in both procedures. The inset graph shows the Drude contribution and the valence intraband contributions at 10 K and 300 K. The valence intraband peak is small and dispersive but is necessary for a good description of the data. Table I lists the 21 parameters used during the fitting routine to fit the reflectance and the conductivity spectra at 300 K.

Figures 10–13 show the temperature dependence of selected parameters from the fits. First, Fig. 10 shows the Drude plasma frequency, whose strength decreases as temperature increases. We also show a plasma frequency calculated from the Hall measurement $\omega_p = \sqrt{4\pi n e^2/m_h^*}$ where n comes from the Hall data and m_h^* from the sum rule analysis for the free carriers. Within the error bars, the two results agree.

Second, the temperature dependence of the central frequencies of the lowest interband transition, the valence intraband transition, and the optical phonon is shown in Fig. 11. The lowest interband transition has its minimum value at 100 ± 25 K. As temperature increases, the valence intraband oscillator shifts towards lower frequencies whereas the phonon mode in the far-infrared range shifts slightly towards higher frequencies.

The linewidth of many of these modes suggests significant overlap amongst them, especially in the midinfrared region. Figure 12 shows the temperature dependence of the linewidth γ of these transitions. The Drude relaxation rate (bottom panel) becomes as small as 17 cm^{-1} (well below our experimental low-frequency limit) at 10 K, increasing with temperature to 195 cm^{-1} at 300 K. The corresponding hole mobility $\mu = e\tau/m_h^*$ decreases from 1630 cm^2/V s at 10 K to 140 cm^2/V s

TABLE I. Drude-Lorentz parameters for $Pb_{0.77}Sn_{0.23}Se$ at room temperature (300 K).

Term in dielectric function	Oscillator strength ω_p (cm^{-1})	Central frequency ω_j (cm^{-1})	Linewidth γ_j (cm^{-1})
Drude	4160	0	195
Optical phonon	240	40	5.5
Valence intraband	1230	550	560
Interband 1	4550	3500	1900
Interband 2	11000	5120	3950
Interband 3	20630	10620	1950
Interband 4	23750	12350	4150

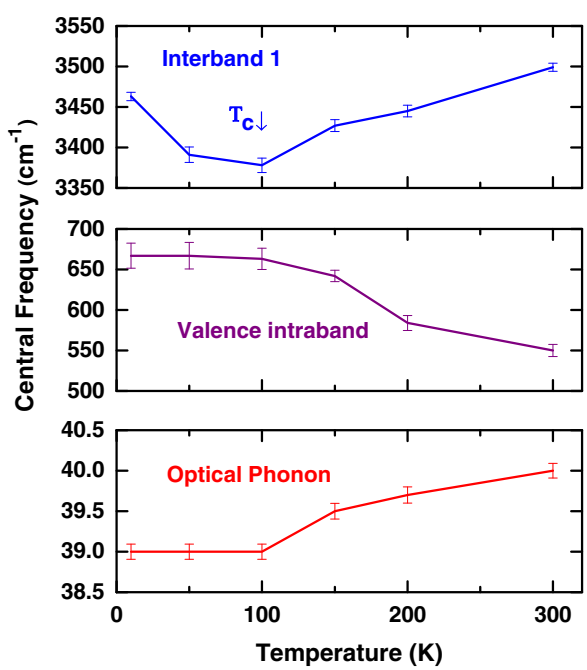

FIG. 11. (Color online) Temperature dependence of the central frequency for the fitted Lorentz oscillators.

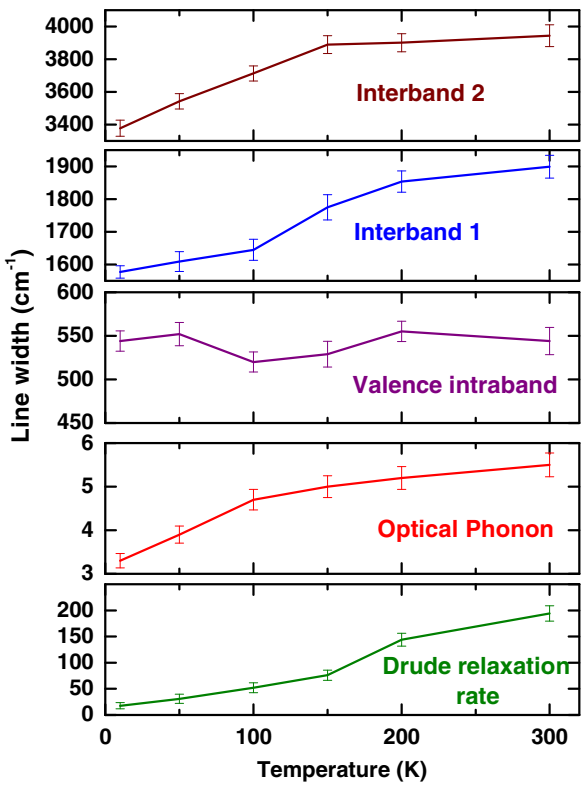

FIG. 12. (Color online) Temperature dependence of the linewidth for the fitted Lorentz oscillators.

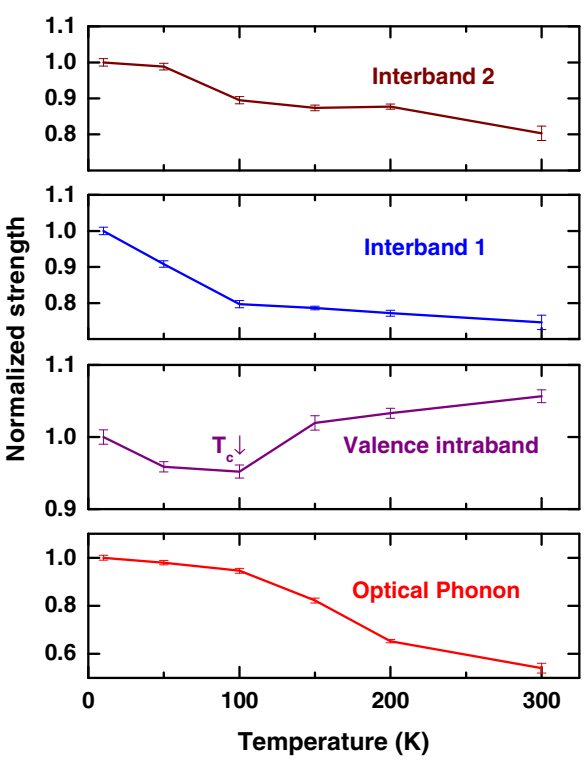

FIG. 13. (Color online) Temperature dependence of the oscillator strength (normalized by the 10 K value) for the fitted Lorentz oscillators.

at 300 K. Based on these hole mobility values, the optical conductivity $\sigma = ne\mu$ is estimated to be 23 200 Ω^{-1} cm^{-1} at 10 K, decreasing to 1320 Ω^{-1} cm^{-1} at 300 K. These estimates are in good agreement with the conductivity values found from the fitting routine: 21 800 Ω^{-1} cm^{-1} at 10 K, decreasing to 1490 Ω^{-1} cm^{-1} at 300 K. The linewidth of every other oscillator shows a similar temperature trend except for the valence intraband mode which has a weak (and not very significant) minimum at 100 K.

Finally, the temperature dependence of the oscillator strength for several oscillators is shown in Fig. 13. The strength has been normalized by its value at 10 K. (The Drude oscillator strength is shown in Fig. 10.) Three oscillators have their highest strength at the lowest temperature; it decreases monotonically as temperature increases, with a change of slope around 100 K. The valence intraband mode is different: it shows a clear minimum at 100 K and is higher at 300 K than at 10 K.

V. DISCUSSION

A. Free-carrier characteristics and band inversion

A scattering rate calculation for a p-type $Si_{1-x}Ge_x$ alloy predicts a quite high scattering rate [35]. Impurity scattering is expected to be strong on account of the disorder associated with the alloy. In contrast, our $Pb_{0.77}Sn_{0.23}Se$ single crystal has a quite small free-carrier scattering rate at low temperature. Indeed, the free-carrier scattering rate (shown in the bottom panel of Fig. 12) remains temperature dependent below 50 K. Considering the alloy form of the material with large stoichiometric imbalance, this result is rather surprising.

Previous studies have shown that the extrinsic carrier density in $Pb_{1-x}Sn_xSe$ affects not only the Hall coefficient but also its temperature dependence. For lightly doped systems, R_H changes sign from positive to negative as temperature is increased, mainly due to the increasing n-type contribution from thermally excited carriers. On the other hand, for heavily doped systems, the Hall coefficient is positive throughout and has weak temperature dependence [15]. As temperature is increased, due to increasing thermal energy, the number of free carriers increases. However an increase in the band gap due to increasing temperature also reduces the number of thermally excited carriers. The value of the Hall coefficient depends on the relative dynamics of these two opposing mechanisms. The slight increase in the Hall coefficient with temperature in our sample could be due to an imbalance between these two competing processes.

Temperature-dependent ARPES measurements of the (100) surface of $Pb_{0.77}Sn_{0.23}Se$ single crystals have been interpreted as finding band inversion in the material around 100 K [17]. The band curvature at the L point changes during band inversion and band dispersion becomes almost linear during gap closure at 100 K. The temperature dependence of the carrier effective mass (shown in Fig. 6) does show a weak minimum, in agreement with this idea.

B. Minimum band gap and the valence intraband transition

The phenomenon of first shrinking and then expansion of band gap as temperature is decreased should affect the

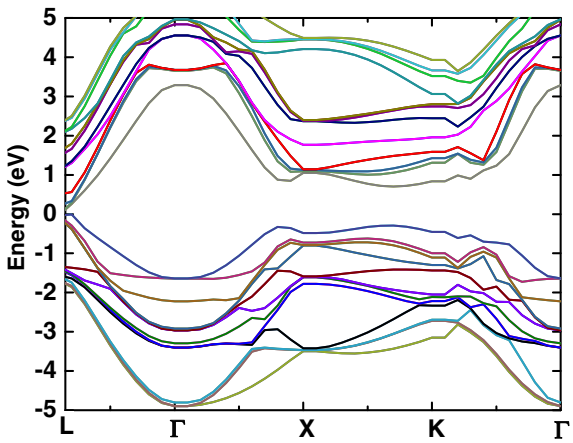

FIG. 14. (Color online) Calculated electronic band structure of $Pb_{0.75}Sn_{0.25}Se$.

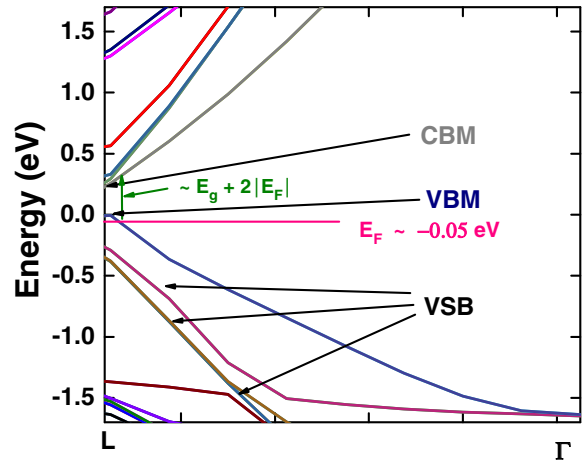

FIG. 15. (Color online) Enlarged view at the L point of the low-energy part of the band structure showing the splitting of the valence band. CBM = conduction band minimum; VBM = valence band maximum; VSB = valence subband.

minimum absorption edge directly. Figure 11 shows that the central frequency of the lowest interband transition has a minimum at 100 K. In addition, the onset of this interband transition, estimated by linear extrapolation of the low-energy edge in the Kramers-Kronig-derived optical conductivity to zero conductivity, suggests a similar trend. An ARPES study also finds a minimum band gap at 100 K [17].

We can point to other features in the optical spectrum that present themselves around 100 K: the frequency of the optically active phonon (Fig. 11) and the linewidth and the spectral weight of the valence intraband transition (Figs. 12 and 13).

C. Electronic structure calculations

The energy band structure of $Pb_{0.75}Sn_{0.25}Se$ was calculated within density functional theory using the VASP package [36–39]. The input structure consists of an 8 atom cell with 3 Pb, 1 Sn, and 4 Se atoms. The calculation was based on a generalized gradient approximation (GGA) for the exchange-correlation potential using the Perdew, Burke, and Ernzerhof formalism [40] along with spin-orbit coupling for both geometric and electronic optimization. We used an energy cutoff of 500 eV, 10^{-6} eV energy minimization, and $8 \times 8 \times 8$ k points. The calculation gave a lattice constant of 6.16 Å, an overestimate by 0.06 Å compared with the measured lattice constant [41]. The electronic band structure was calculated along high-symmetry k points in the Brillouin zone with the Fermi energy fixed to zero (i.e., an undoped crystal). As shown in Fig. 14, the band structure calculation indicates that the material has a direct band gap at the L point in the Brillouin zone with an energy gap of 0.20 eV. Figure 15 shows an enlarged view of the conduction band minimum and the valence band maximum at the L point.

The spin-orbit interaction is important in determining the actual band ordering, band splitting, and the details of the electronic structure in class IV-VI narrow-gap semiconductors. Figure 15 shows the splitting of the valence band into three valence subbands. By analogy to the valence bands of tetrahedrally coordinated semiconductors, we can call these "light-hole," "heavy-hole," and "split-off" bands [42,43].

This VASP calculation also produced the density of states. Using the carrier density from experiment and this density of states under a rigid-band approximation, we found that the Fermi energy in our doped sample lies around $E_F = -50$ meV. The corresponding energy of the onset of the absorption associated with the lowest interband transition which takes place from E_{Fi} in the valence band to the empty state in the conduction band at the same k point could be estimated to be equal to $E_g + 2\,|E_F\,|$. This increase in the optical gap due to an extrinsic carrier density is known as the Burstein-Moss shift [44,45]. Apart from lead salts such as PbTe and PbSe, the Burstein-Moss shift in optical conductivity has been reported in many other class III-V semiconductors and their mixed alloys [46,47]. Our band-structure calculation predicts this absorption to start around 0.30 eV (2420 cm^{-1}). This prediction is in good agreement with the estimate of 2300 cm^{-1} from the threshold for the interband transitions seen in the optical conductivity.

In addition to the optical interband transitions between the valence and the conduction band, there are also optical transitions within the valence band: the valence intraband transition discussed above. These transitions are seen in a number of p-type semiconductors, when the top of the valence band is populated with holes. It is then possible to make intraband transitions within the valence band from low-lying subbands to states above the Fermi level. These transitions have been observed in a number of semiconductors, including Ge, GaAs, and InSb [48–50]. The single crystal of $Pb_{0.77}Sn_{0.23}Se$ shows similar valence intraband transitions whose temperature dependence is shown in Figs. 11–13.

VI. CONCLUSIONS

Hall measurements of $Pb_{0.77}Sn_{0.23}Se$ single crystals disclose the p-type nature of the material and show that the carrier density decreases from 9×10^{19} cm^{-3} at 10 K to 6×10^{19} cm^{-3} at 300 K. Temperature-dependent optical reflectance measurement shows degenerate semiconductor

behavior. At 10 K, the screened Drude plasma minimum lies around 930 cm^{-1}; it shifts slightly towards lower frequency as temperature increases.

In the midinfrared and near-infrared region, the spectra show valence intraband transition and valence to conduction band excitations. The temperature dependence of the lowest-energy interband transition energy shows a minimum at 100 K. This behavior suggests band inversion in the material, also predicted by many other previous studies. The effective hole mass also has a minimum value at 100 K consistent with linear band dispersion at the L point in the Brillouin zone. Theoretical calculations provide the details of electronic band structure, supporting the existence of a valence intraband transition. Our experimental and theoretical studies suggest that the material undergoes a temperature-driven band inversion at the L point as also predicted by previous studies [17,18].

ACKNOWLEDGMENTS

The authors wish to thank Xiaoxiang Xi for his constructive discussions on the band structure of the material. This work was supported by the DOE through Contract No. DE-AC02-98CH10886 at Brookhaven National Laboratory and by NSF DMR 1305783 (A.F.H.).

[1] G. Nimtz and B. Schlicht, *Narrow-Gap Semiconductors*, Springer Tracts in Modern Physics, Vol. 98 (Springer, Berlin, 1983), pp. 1–117.
[2] A. A. Reijnders, J. Hamilton, V. Britto, J.-B. Brubach, P. Roy, Q. D. Gibson, R. J. Cava, and K. S. Burch, Phys. Rev. B **90**, 235144 (2014).
[3] O. Madelung, *Semiconductors: Data Handbook* (Springer, Berlin, 2004), pp. 566–605.
[4] J. O. Dimmock, I. Melngailis, and A. J. Strauss, Phys. Rev. Lett. **16**, 1193 (1966).
[5] L. Fu, Phys. Rev. Lett. **106**, 106802 (2011).
[6] T. H. Hsieh, H. Lin, J. Liu, W. Duan, A. Bansil, and L. Fu, Nat. Commun. **3**, 982 (2012).
[7] X. Xi, X.-G. He, F. Guan, Z. Liu, R. D. Zhong, J. A. Schneeloch, T. S. Liu, G. D. Gu, X. Du, Z. Chen, X. G. Hong, W. Ku, and G. L. Carr, Phys. Rev. Lett. **113**, 096401 (2014).
[8] M. Cardona and D. L. Greenaway, Phys. Rev. **133**, A1685 (1964).
[9] S. E. Kohn, P. Y. Yu, Y. Petroff, Y. R. Shen, Y. Tsang, and M. L. Cohen, Phys. Rev. B **8**, 1477 (1973).
[10] D. E. Aspnes and M. Cardona, Phys. Rev. **173**, 714 (1968).
[11] A. Delin, P. Ravindran, O. Eriksson, and J. M. Wills, Int. J. Quantum Chem. **69**, 349 (1998).
[12] T. C. Harman and I. Melngailis, Appl. Solid State Sci. **4**, 1 (1974).
[13] W. Albers, C. Haas, H. Ober, G. Schodder, and J. Wasscher, J. Phys. Chem. Solids **23**, 215 (1962).
[14] P. B. Littlewood, B. Mihaila, R. K. Schulze, D. J. Safarik, J. E. Gubernatis, A. Bostwick, E. Rotenberg, C. P. Opeil, T. Durakiewicz, J. L. Smith, and J. C. Lashley, Phys. Rev. Lett. **105**, 086404 (2010).
[15] J. R. Dixon and G. F. Hoff, Phys. Rev. B **3**, 4299 (1971).
[16] A. J. Strauss, Phys. Rev. **157**, 608 (1967).
[17] P. Dziawa, B. J. Kowalski, K. Dybko, R. Buczko, A. Szczerbakow, M. Szot, E. Łusakowska, T. Balasubramanian, B. M. Wojek, M. H. Berntsen, O. Tjernberg, and T. Story, Nat. Mater. **11**, 1023 (2012).
[18] B. M. Wojek, R. Buczko, S. Safaei, P. Dziawa, B. J. Kowalski, M. H. Berntsen, T. Balasubramanian, M. Leandersson, A. Szczerbakow, P. Kacman, T. Story, and O. Tjernberg, Phys. Rev. B **87**, 115106 (2013).
[19] X. Gao and M. S. Daw, Phys. Rev. B **77**, 033103 (2008).
[20] S. I. Novikova and N. Kh. Abrikosov, Sov. Phys. Solid State **5**, 1397 (1964).
[21] G. Martinez, Phys. Rev. B **8**, 4686 (1973).
[22] H. Maier and D. Daniel, J. Electron. Mater. **6**, 693 (1977).
[23] C. Julien, M. Eddrief, I. Samaras, and M. Balkanski, Mater. Sci. Eng. B **15**, 70 (1992).
[24] A. J. Strauss and R. F. Brebrick, J. Phys. Colloques **29**, C4-21 (1968).
[25] S. Asanabe, J. Phys. Soc. Jpn. **14**, 281 (1959).
[26] A. E. Goldberg and G. R. Mitchell, J. Chem. Phys. **22**, 220 (1954).
[27] J. Habinshuti, O. Kilian, O. Cristini-Robbe, A. Sashchiuk, A. Addad, S. Turrell, E. Lifshitz, B. Grandidier, and L. Wirtz, Phys. Rev. B **88**, 115313 (2013).
[28] B. L. Wehrenberg, C. Wang, and P. Guyot-Sionnest, J. Phys. Chem. B **106**, 10634 (2002).
[29] F. Wooten, *Optical Properties of Solids* (Academic Press, New York, 1972).
[30] B. Henke, E. Gullikson, and J. Davis, At. Data Nucl. Data Tables **54**, 181 (1993).
[31] D. B. Tanner, arXiv:1411.2061.
[32] J. O. Dimmock and G. B. Wright, Phys. Rev. **135**, A821 (1964).
[33] J. Wu, W. Walukiewicz, W. Shan, K. M. Yu, J. W. Ager, E. E. Haller, H. Lu, and W. J. Schaff, Phys. Rev. B **66**, 201403 (2002).
[34] P. Perlin, E. Litwin-Staszewska, B. Suchanek, W. Knap, J. Camassel, T. Suski, R. Piotrzkowski, I. Grzegory, S. Porowski, E. Kaminska, and J. C. Chervin, Appl. Phys. Lett. **68**, 1114 (1996).
[35] S. Joyce, F. Murphy-Armando, and S. Fahy, Phys. Rev. B **75**, 155201 (2007).
[36] G. Kresse and J. Hafner, Phys. Rev. B **47**, 558 (1993).
[37] G. Kresse and J. Hafner, Phys. Rev. B **49**, 14251 (1994).
[38] G. Kresse and J. Furthmüller, Comput. Mater. Sci. **6**, 15 (1996).
[39] G. Kresse and J. Furthmüller, Phys. Rev. B **54**, 11169 (1996).
[40] J. P. Perdew, K. Burke, and M. Ernzerhof, Phys. Rev. Lett. **77**, 3865 (1996).
[41] P. Haas, F. Tran, and P. Blaha, Phys. Rev. B **79**, 085104 (2009).

[42] J. Pankove, *Optical Processes in Semiconductors* (Dover Publications, Inc., New York, NY, 1975).
[43] R. Braunstein and E. Kane, J. Phys. Chem. Solids **23**, 1423 (1962).
[44] E. Burstein, Phys. Rev. **93**, 632 (1954).
[45] T. S. Moss, Proc. Phys. Soc., London, Sect. B **67**, 775 (1954).
[46] F. Stern, J. Appl. Phys. **32**, 2166 (1961).
[47] Z. M. Gibbs, A. LaLonde, and G. J. Snyder, New J. Phys. **15**, 075020 (2013).
[48] W. Kaiser, R. J. Collins, and H. Y. Fan, Phys. Rev. **91**, 1380 (1953).
[49] G. W. Gobeli and H. Y. Fan, Phys. Rev. **119**, 613 (1960).
[50] M. Grundmann, *The Physics of Semiconductors* (Springer, Berlin, 2006), pp. 213–249.